[3]D.J. Gibbons, *Handbook of Vacuum Physics* (Pergamon, New York, 1966), Vol. 2.
[4]J.B. Smith, Rev. Sci. Instr. (to be published).
[5]J.R. Prescott, Nucl. Instr. Methods **39**, 173 (1966).
[6]R.E. Barrington and J.M. Anderson, Proc. Phys. Soc. (London) B72, 717 (1958).
[7]W.H. Wright, Brit. J. Appl. Phys. 2, 895 (1969).

Electrostatic-Inertial Plasma Confinement*

T.J. Dolan,† J.T. Verdeyen, D.J. Meeker, and B.E. Cherrington
Gaseous Electronics Laboratory, University of Illinois, Urbana, Illinois 61801
(Received 9 June 1971; in final form 13 December 1971)

Electrostatic-inertial plasma confinement consists of trapping charged particles in potential wells of the electric field, which are created by ions or electrons injected radially inwards into a hollow sphere or cylinder. Theoretical expressions are derived for the potential and particle densities as functions of radius, grid voltage, and current. A neon plasma is produced in cylindrical geometry, using a grid 4 cm in diameter and 16 cm long. Using the laser heterodyne technique at 0.6401 and 0.6328 μ, the density of neon atoms in the $1s_5$ metastable state is measured (10^9—10^{12} cm^{-3}) as a function of radial position, time, grid current (20 —μsec pulses of up to 4 A), grid voltage (0.2 — 3.0 kV), gas pressure (0.001 — 0.01 Torr), and grid mesh spacing, and compared with theoretical predictions. The peak electron density is 10^{11} cm^{-3}. When the spacing between grid wires is larger than 1 mm, a decrease in metastable density, attributed to the presence of a plasma sheath around the grid wires, is observed. The radial variation of plasma light intensity is compared with the theoretical radial distribution of electron density.

I. INTRODUCTION

This work is directed towards an answer to the question: "How dense a plasma can be confined by electrostatic-inertial means?" Electrostatic-inertial plasma confinement consists of trapping charged particles in potential wells of the electric field, which are produced by ions or electrons injected radially inwards into a hollow sphere or cylinder.[1–4] Interest in this method was stimulated by experimental results of Hirsch[3] in which neutron yields of about 10^{10} sec^{-1} were observed, apparently from D-T reactions in an electrostatically confined plasma.

Simplified calculations, assuming monoenergetic particles with zero angular momentum, indicate a spatially oscillatory potential with trapping of both ions and electrons in their respective wells.[3] Such a potential configuration might be the basis for high-density plasma confinement if it could be produced in practice. An approximate solution by Lavrent'yev including effects of energy spread and angular momentum in spherical geometry indicated only one potential well with a broad flat bottom.[2] In this paper the theory is further developed for comparison with the present experimental results.

In practice, a highly open wire mesh grid in the form of a sphere or cylinder is biased at a high negative (or positive) voltage to accelerate ions (or electrons) radially inwards. Since the grid mesh is highly open, most of the accelerated particles pass through the grid several times, oscillating in and out, before being intercepted by it. These particles are "injected" into the region inside the grid where they can produce ionizations in the neutral gas. The space charge of the injected particles produces a potential well which traps charged particles of the opposite sign, as indicated in Fig. 1 where r_g = grid radius. For certain cases of the particle energy distributions, it might be possible to produce a second potential well of opposite polarity inside the first well (a spatially oscillatory potential), so that both ions and electrons could be trapped in different potential wells, isolated from contact with the grid.

The particle energy distribution functions depend upon many complex factors, including ionization, charge exchange, interparticle collisions, particle deflections at the grid, particle loss to the grid, particle emission from the grid, recombination of ions and electrons, and loss of particles which are too energetic to be trapped. The present work attempts to find solutions of Poisson's equation in spherical and cylindrical geometries for assumed distribution functions of total energy and angular momentum. From the potential solutions the radial variations of electron density and ion density are obtained.

The main diagnostic method used was to measure the spatial distribution of neon $1s_5$ metastable atoms in a neon plasma and compare the measured values with those predicted using the theoretical electron density distributions. The other diagnostic technique employed was measurement of the intensity of the light emitted by the plasma as a function of radius, using a collimated phototube. The light observed is mainly excited light from atomic states with short lifetimes, so that its

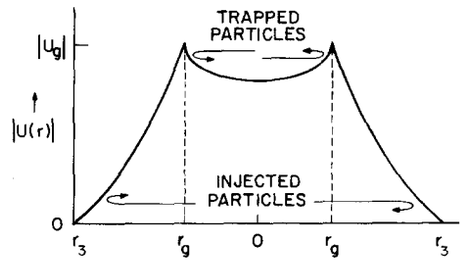

FIG. 1. Potential vs radius.

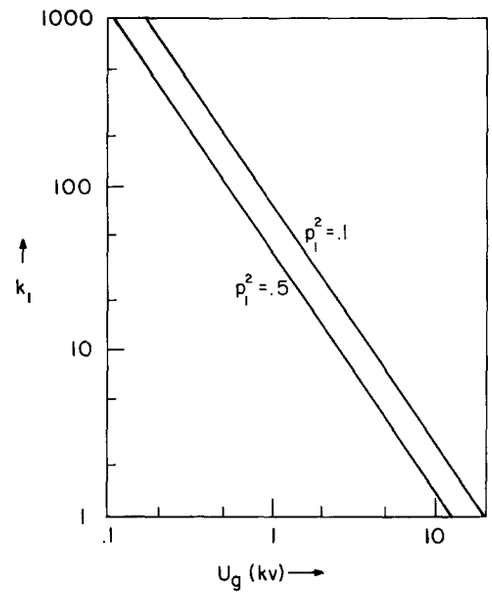

FIG. 2. Dimensionless current vs grid voltage for Ne^+ ion injection, assuming $y_5 = 0$, $y_6 = 1$, $I_1 = 1$ A, $r_g = 2$ cm, and $l = 15$ cm.

radial distribution should have the same shape as the theoretical electron density distribution. Although the experimental work was done using neon and deuterium, the results should be applicable to other gases as well, since the solutions of Poisson's equation are applicable to ions of any mass.

II. POTENTIAL DISTRIBUTION

The potential as a function of radius will be found for spherical and cylindrical geometries, assuming symmetry in other spatial variables, and ignoring effects of collisions and reactions, such as ionization. The method of Lavrent'yev[2] is followed, whereby Poission's equation is solved together with the equations of motion for the ions and electrons.

In the following analysis, the subscripts 1 and 2 will refer to the injected and trapped particles, respectively. (For the case where ions are being injected through the grid, the subscript 1 refers to ions, and the subscript 2 to electrons.) The subscript g will refer to the grid, and the subscripts r and ϕ will refer to radial and angular components of velocity.

A charged particle in the system under consideration has two constants of motion: its total energy (defined as the sum of its kinetic and potential energies) and its angular momentum (which is conserved, since the forces act only radially in this model). The nonrelativistic conservation equations are

$$\begin{aligned} &\tfrac{1}{2}m_1v_{1r}^2 + \tfrac{1}{2}m_1v_{1\phi}^2 + q_1U(r) = q_1W_1 = \text{const}, \\ &\qquad m_1rv_{1\phi} = L_1 = \text{const}, \\ &\tfrac{1}{2}m_2v_{2r}^2 + \tfrac{1}{2}m_2v_{2\phi}^2 + q_2U(r) = q_2W_2 = \text{const}, \\ &\qquad m_2rv_{2\phi} = L_2 = \text{const}, \end{aligned} \tag{1}$$

where m = mass (kg), q = charge (C), U = potential (V), W = total energy (V), L = angular momentum (kg m^2 sec^{-1}), v = velocity (m sec^{-1}), and r = radius (m).

The radial velocities are found to be

$$\begin{aligned} v_{1r} &= (-2q_1U_g/m_1)^{1/2}[y(x) - y_1 - \xi_1^2/x^2]^{1/2} \\ &\qquad (q_1 \text{ and } U_g \text{ have the opposite sign}), \\ v_{2r} &= (2q_2U_g/m_2)^{1/2}[y_2 - y(x) - \xi_2^2/x^2]^{1/2}, \end{aligned} \tag{2}$$

where $x = r/r_g$; $y = U/U_g$; $y_{1,2} = W_{1,2}/U_g$ is the dimensionless total energy; $\xi_1 = [L_1^2/2m_1r_g^2(-q_1U_g)]^{1/2}$ is the dimensionless angular momentum; and

$$\xi_2 = (L_2^2/2m_2r_g^2q_2U_g)^{1/2}.$$

A typical potential distribution is sketched in Fig. 1. In order to stay in the system a significant amount of time, a particle's total energy $y_{1,2}$ must be between 0 and 1. In order to avoid negative arguments of the square roots in Eq. (2), it is required that $y_1 \leq y \leq y_2$. Therefore,

$$0 \leq y_1 \leq y(x) \leq y_2 \leq 1. \tag{3}$$

The possible values of angular momentum ξ which a particle can have at a given radius x lie between zero and $\xi_{\max}$, which is found by setting $v_r = 0$:

$$\begin{aligned} 0 \leq \xi_1 \leq \xi_{1\max} &= x(y - y_1)^{1/2}, \\ 0 \leq \xi_2 \leq \xi_{2\max} &= x(y_2 - y)^{1/2}. \end{aligned} \tag{4}$$

Equations (3) and (4) describe the limiting values of total energy and angular momentum which a particle can have at a given radius. These values will be the limits of integration in relating the particle densities at a given radius to the distribution functions.

The distribution of particles will be described in terms of the constants of motion, $\xi_{1,2}$ and $y_{1,2}$. Let N_1 be the total number of injected particles inside the system, bounded by some radius r_3, and let $g_1(\xi_1, y_1)\,d\xi_1\,dy_1$ be the number of injected particles anywhere in the system having angular momentum and total energy in $d\xi_1$ and dy_1 at ξ_1, y_1. Then,

$$N_1 = \int_0^\infty dy_1 \int_0^\infty d\xi_1 g_1(\xi_1, y_1), \tag{5}$$

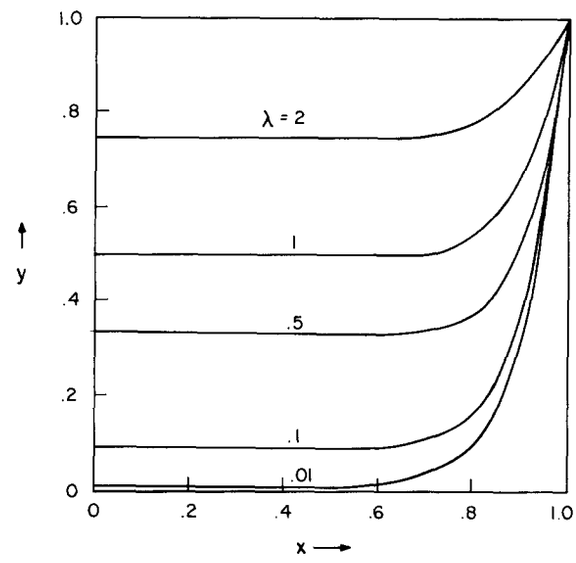

FIG. 3. Potential vs radius, spherical geometry. $y_5 = 0$, $y_6 = 0.5$, $y_7 = 0$, $y_8 = 1$, $p_1^2 = p_2^2 = 0.5$, and $k_1 = 100$.

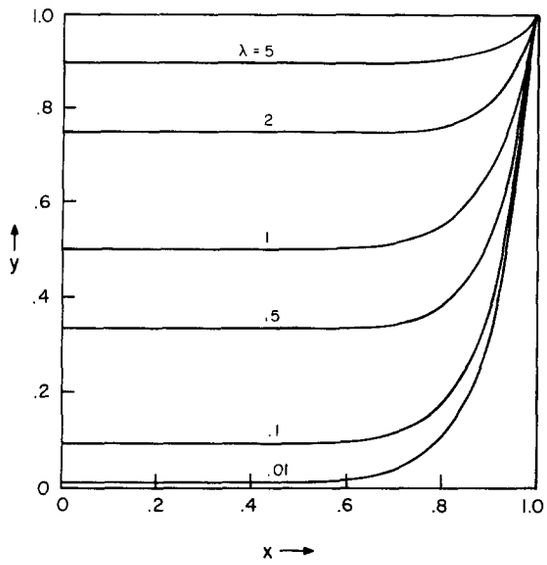

FIG. 4. Potential vs radius, cylindrical geometry. $y_5=0$, $y_6=0.5$, $y_7=0$, $y_8=1$, $p_1^2=p_2^2=0.5$, and $k_1=100$.

where g_1 will be zero for impossible values of ξ_1, y_1.

Consider a thin spherical shell with volume $4\pi r^2 dr$. Some of the injected particles may oscillate in and out with a period of oscillation given by

$$\tau_1 = 2\int_{r_{\min}}^{r_{\max}} dr/v_{1r}(r), \tag{6}$$

where $r_{\min}$ and $r_{\max}$ are found from the equations of motion. The fraction of time that a particle is present in the shell is

$$\frac{dt}{\tau_1} = \frac{2dr}{v_{1r}\tau_1}\,u(r-r_{\min})\,u(r_{\max}-r), \tag{7}$$

where $u(\ )$ is the unit step function

$$u(x) = \begin{cases} 0, & x<0 \\ 1, & x>0. \end{cases}$$

The factor 2 represents the fact that a particle passes through the shell twice during each full period of oscillation. The differential density of injected particles in the shell is therefore

$$f_1(r,\ \xi_1,\ y_1)\,d\xi_1\,dy_1 = \frac{[g_1(\xi_1,\ y_1)\,d\xi_1\,dy_1][2\,dr\,u(r-r_{\min})\,u(r_{\max}-r)/v_{1r}\tau_1]}{4\pi r^2\,dr}, \tag{8}$$

where $g_1(\xi_1,\ y_1)\,d\xi_1\,dy_1$ is the number of injected particles with momenta and energies in $d\xi_1$ and dy_1 at ξ_1, y_1; $2\,dr\,u(r-r_{\min})u(r_{\max}-r)/v_{1r}\tau_1$ is the fraction of time that each particle spends in the shell; and $4\pi r^2 dr$ is the volume of the shell.

The injected particle density is

$$n_1(r) = \int_0^\infty dy_1 \int_0^\infty d\xi_1 f_1(\xi_1,\ y_1). \tag{9}$$

A simple check for consistency of the above definitions can be made by noting that the integral of the injected particle density, n_1, over the volume $0-r_3$ is equal to N_1.

The step functions in Eq. (8) represent the restrictions of the equations of motion upon the particles which may be present at a given radius. They may be replaced by conditions (3) and (4), which express the same restrictions in terms of ξ_1 and y_1.

Combining Eqs. (2), (8), and (9), and using conditions (3) and (4) on the limits of integration, the density of injected particles is found to be

$$n_1(r) = \int_0^y dy_1 \times \int_0^{\xi_{1\max}} d\xi_1 \frac{2g_1(\xi_1,\ y_1)}{4\pi r^2\tau_1(-2q_1U_g/m_1)^{1/2}(y-y_1-\xi_1^2/x^2)^{1/2}}. \tag{10}$$

Since the period τ_1 is a complicated function of the unknown potential $y(x)$, it is desirable to avoid calculating τ_1 during solution of Poisson's equation. Therefore, a current distribution function i will be defined by

$$i_1(\xi_1,\ y_1)\,d\xi_1\,dy_1 = 2q_1 g_1(\xi_1,\ y_1)d\xi_1 dy_1/\tau_1 \ \text{(A)}. \tag{11}$$

This function represents the inward and outward flow of charges with energies and momenta in dy_1 and $d\xi_1$ at ξ_1, y_1 per unit time. The total two-way charge flow, or "circulating current" I_1 of injected particles at the grid ($x=1$) is found by summing over all energies and angular momenta:

$$I_1 = \int_0^1 dy_1 \int_0^{(1-y_1)^{1/2}} d\xi_1\,|i_1(\xi_1,\ y_1)|. \tag{12}$$

This circulating current is related to the measured grid current I by[4]

$$I_1/I = 2\epsilon/(1-\epsilon^2), \tag{13}$$

where ϵ is the effective openness of the grid $\leq$ (open area of grid)/(total area of grid).

Combining Eqs. (10) and (11), the density of injected particles is

$$n_1(x) = \int_0^y dy_1 \times \int_0^{\xi_{1\max}} d\xi_1 \frac{i_1(\xi_1,\ y_1)}{4\pi r_g^2 x^2 q_1(-2q_1U_g/m_1)^{1/2}(y-y_1-\xi_1^2/x^2)^{1/2}}. \tag{14}$$

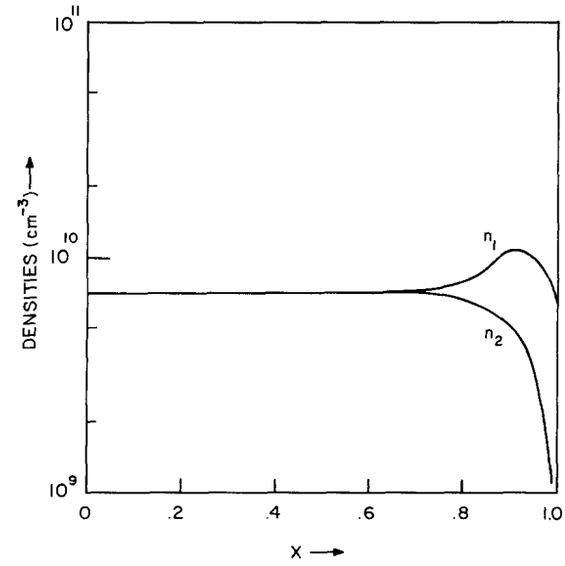

FIG. 5. Cylindrical geometry, density vs radius. $y_5=0$, $y_6=0.5$, $y_7=0$, $y_8=1$, $k_1=100$, $\lambda=0.5$, $p_1^2=p_2^2=0.5$, Ne^+ ion injection at 1000 V, $r_g=2$ cm, and $I_1=1.44$ A.

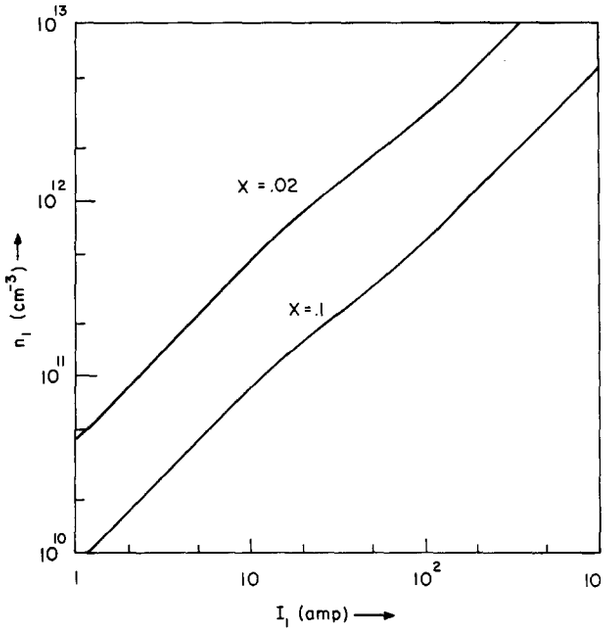

FIG. 6. Density vs current, spherical geometry. $y_5=0$, $y_6=0.5$, $y_7=0$, $y_8=1$, $\lambda=0.5$, $p_1^2=p_2^2=0.5$, deuterium ion injection at $U_g=10^5$ V, and $r_g=2$ cm.

Similarly, the density of the trapped particles is found by making the following permutations: subscript $1\rightarrow 2$; $(y-y_1)\rightarrow(y_2-y)$; $\int_0^y \rightarrow \int_y^1$; and $-q_1\rightarrow q_2$.

Using Eq. (14) with definitions from (2), Poisson's equation becomes

$$\frac{d}{dx}(x^2y')=Q_1(x,\ y)-Q_2(x,\ y), \tag{15}$$

where $y'=dy/dx$,

$$Q_1(x,\ y)=\int_0^y dy_1\int_0^{\xi_{1\max}} d\xi_1\,\frac{h_1(\xi_1,\ y_1)}{[y-y_1-\xi_1^2/x^2]^{1/2}},$$

$$h_1(\xi_1,\ y_1)=\frac{m_1^{1/2}}{4\pi\epsilon_0(-2q_1U_g)^{1/2}}\left(\frac{-i_1(\xi_1,\ y_1)}{U_g}\right),$$

and Q_2 and h_2 are found from Q_1 and h_1 by means of the above permutations. The boundary conditions are $y'(0)=0$ and $y(1)=1$. Equation (15) is equivalent to one derived by Lavrent'yev.[2]

For cylindrical geometry, a similar result is obtained:

$$\frac{d}{dx}(xy')=R_1(x,\ y)-R_2(x,\ y),$$
$$R_{1,2}(x,\ y)=\frac{2r_g}{l}Q_{1,2}(x,\ y), \tag{16}$$

where $l=$ length of cylindrical plasma (m) and the boundary conditions are the same.

The partical densities are found to be

$$\text{(spherical) } n_{1,2}(x)=\frac{\epsilon_0}{r_g^2}\left|\frac{U_g}{q_{1,2}}\right|\frac{Q_{1,2}(x,\ y)}{x^2},$$
$$\text{(cylindrical) } n_{1,2}(x)=\frac{\epsilon_0}{r_g^2}\left|\frac{U_g}{q_{1,2}}\right|\frac{R_{1,2}(x,y)}{x}. \tag{17}$$

The potential variation can now be found for arbitrary distribution functions of the particles. Rectangular distribution functions appear to be reasonable approximations to the apparent steady-state distributions found by Barnes[5] and Dunn,[6] and they permit immediate integration over $y_{1,2}$ and $\xi_{1,2}$. The rectangular distributions represent uniform spread of angular momenta between zero and some maximum value p_1, p_2 and uniform total energies from y_5 to y_6 and y_7 to y_8:

$$h_1(\xi_1,\ y_1)=k_1u(y_1-y_5)\,u(y_6-y_1)\,u(p_1-\xi_1),$$
$$h_2(\xi_2,\ y_2)=k_2u(y_2-y_7)\,u(y_8-y_2)\,u(p_2-\xi_2), \tag{18}$$
$$(0\le y_5\le y_6\le 1,\quad 0\le y_7\le y_8\le 1,\quad 0\le p_1\le 1,\quad 0\le p_2\le 1),$$

where k_1 and k_2 are dimensionless constants which are related to the currents of injected and trapped particles. From Eq. (12), with the definition of h_1 from (15), we have

$$\int_0^1 dy_1\int_0^{(1-y_1)^{1/2}} d\xi_1\,h_1(\xi_1,\ y_1)$$
$$=(m_1^{1/2}/4\pi\epsilon_0|2q_1|^{1/2}|U_g|^{3/2})\,I_1. \tag{19}$$

Evaluating the same integral using Eq. (18) and solving for k_1 yields

$$k_1=\frac{m_1^{1/2}}{4\pi\epsilon_0|2q_1|^{1/2}|U_g|^{3/2}}\frac{I_1}{C_1}, \tag{20}$$

where

$$C_1=p_1u(1-p_1^2-y_5)[\min(y_6,\ 1-p_1^2)-y_5]$$
$$+\tfrac{2}{3}u(y_6-1+p_1^2)\{[1-\max(y_5,\ 1-p_1^2)]^{3/2}-(1-y_6)^{3/2}\};$$

min and max denote functions which select the smallest and largest of their arguments.

Equations (20) and (13) relate the constant k_1 to the experimentally measured grid current and voltage. The constant k_2 cannot be so easily defined, because the limits of integration for i_2 would depend upon the shape of the potential distribution. Figure 2 shows the value of k_1 for Ne^+ ion injection assuming $I_1=1$ A. (Neon ions

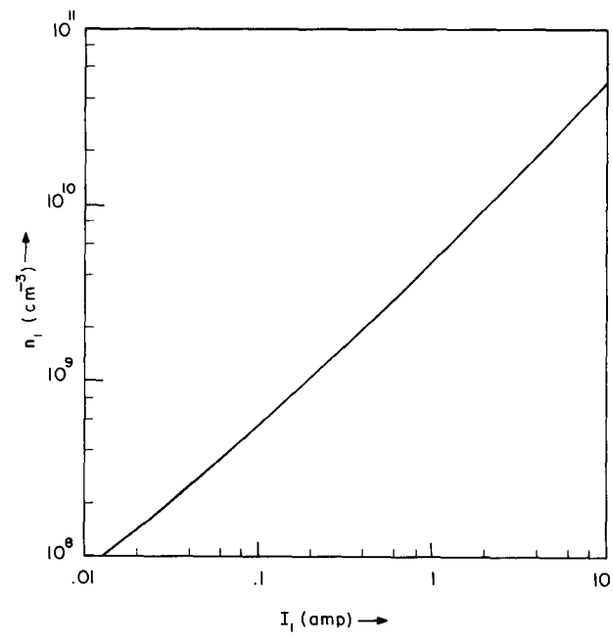

FIG. 7. Axial density vs current, cylindrical geometry. Ne^+ ion injection at 1000 V, $r_g=2$ cm, $y_5=0$, $y_6=0.5$, $y_7=0$, $y_8=1$, $\lambda=0.5$, and $p_1^2=p_2^2=0.5$.

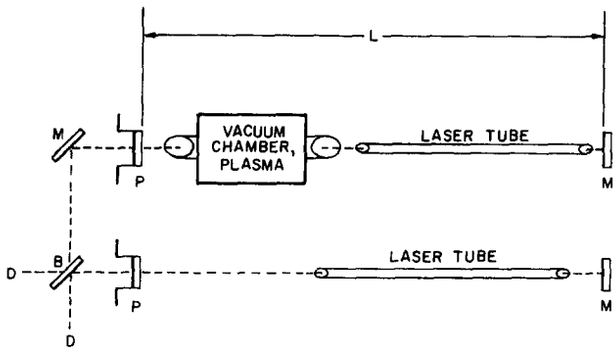

FIG. 8. Laser heterodyne system. M—mirror, P—mirror mounted in piezoelectric crystal, B—beam splitter, D—optical detector, and L—length of laser cavity containing plasma.

were used in the experiment.) Let

$$\lambda = k_2/k_1. \tag{21}$$

In the present work, various values of λ will be assumed, and the resultant potential distributions found.

Using Eqs. (18) and (15) and integrating over angular momentum and total energy, the terms on the right-hand side of Poisson's equation are found to be

$$Q_1(x, y) = k_1 x u(y - y_5)\left\{\frac{\pi}{2} u\left(y_6 - y - \frac{p_1^2}{x^2}\right)\right.$$
$$\times\left[\min(y, y_6) - \max\left(y_5, y - \frac{p^2}{x^2}\right)\right] + \frac{p_1^2}{x^2} u\left(y - \frac{p_1^2}{x^2} - y_5\right)$$
$$\left.\times\left(\frac{\sin^{-1}\psi_1}{\psi_1^2} - \frac{\sin^{-1}\psi_2}{\psi_2^2} + \frac{(1-\psi_1^2)^{1/2}}{\psi_1} - \frac{(1-\psi_2^2)^{1/2}}{\psi_2}\right)\right\},$$
$$Q_2(x, y) = \lambda k_1 x u(y_8 - y)\left\{\frac{\pi}{2} u\left(y + \frac{p_2^2}{x^2} - y_7\right)\right. \tag{22}$$
$$\times\left[\min\left(y_8, y + \frac{p_2^2}{x^2}\right) - \max(y, y_7)\right] + \frac{p_2^2}{x^2} u\left(y_8 - y - \frac{p_2^2}{x^2}\right)$$
$$\left.\times\left(\frac{\sin^{-1}\psi_3}{\psi_3^2} - \frac{\sin^{-1}\psi_4}{\psi_4^2} + \frac{(1-\psi_3^2)^{1/2}}{\psi_3} - \frac{(1-\psi_4^2)^{1/2}}{\psi_4}\right)\right\},$$

where

$$\psi_1 = p_1/x(y - y_5)^{1/2}, \quad \psi_1 = p_1\{x[y - \min(y_6, y - p_1^2/x^2)]^{1/2}\}^{-1},$$
$$\psi_3 = p_2/x(y_8 - y)^{1/2}, \quad \psi_4 = p_2\{x[\max(y_7, y + p_2^2/x^2) - y]^{1/2}\}^{-1}.$$

[For the special case of zero angular momentum and infinitesimally narrow energy spreads, the Poisson equation can be reduced down to a simpler form by setting $y_5 = 0$, $y_8 = 1$, taking the limit as $y_6 \to y_5$, $y_7 \to y_8$, $p_1 \to 0$, $p_2 \to 0$, and using the definition of the derivative in the form

$$\lim_{\zeta \to 0}\left(\frac{f(y) - f(y-\zeta)}{\zeta}\right) = \frac{df(y)}{dy}. \tag{23}$$

Poisson's equation then reduces to

$$\frac{d}{dx}(x^2 y') = K[y^{-1/2} - (1-y)^{-1/2}], \tag{24}$$

where

$$K = m_1^{1/2} I_1/4\pi\epsilon_0 |2q_1|^{1/2} |U_g|^{3/2}, \quad \lambda = m_2^{1/2} I_2/m_1^{1/2} I_1.$$

Equation (24) is the equation solved by Hirsch,[3] yielding a spatially oscillatory potential.]

Using the rectangular distribution functions, the Poisson equations (15) and (16) with $Q_{1,2}$ from Eq. (22) have been solved numerically using the shooting method with a fourth-order Runge-Kutta approximation.[7] The integration step sizes used were 0.001—0.01, with initial steps of 10^{-6}—10^{-4}. The effect of varying λ is shown in Figs. 3 and 4. Note the relatively flat bottom of the potential well. An increase in current (k_1) results in an increase of potential well depth. These curves are similar to the curve predicted by Lavrent'yev[2] and to those observed in computer simulations of plasma by Barnes.[5]

The relative electron and ion densities as a function of radius corresponding to the above potential distributions are shown in Fig. 5.

For high currents, the densities are equal at $x = 0$. The theoretical plasma density, given in Figs. 6 and 7, is approximately linear with current, except at low currents.

By varying the angular momentum spread p_1 of the injected particles, assuming $p_2 = p_1$, it is found that the plasma density near the center varies roughly as p_1^{-1}, in agreement with the predictions of Lavrent'yev.[2] This variation with angular momentum spread indicates the importance of good focusing for the confinement of high-density plasma.

In an attempt to explain the results of the Hirsch[3] experiments, the energy spread of the injected particles and the angular momentum spreads were made very narrow, to simulate the well-focused ion guns used in those experiments. Using $U_g = 10^5$ V, $I = 0.06$ A, $I_1 = 10I$, $\lambda = 0.5$, and $r_g = 5.7$ cm, the resultant density at $r = 1$ mm is less than 10^{12} cm^{-3}, which gives a theoretical neutron yield much lower than the experimentally observed value. There are several reasons why the pres-

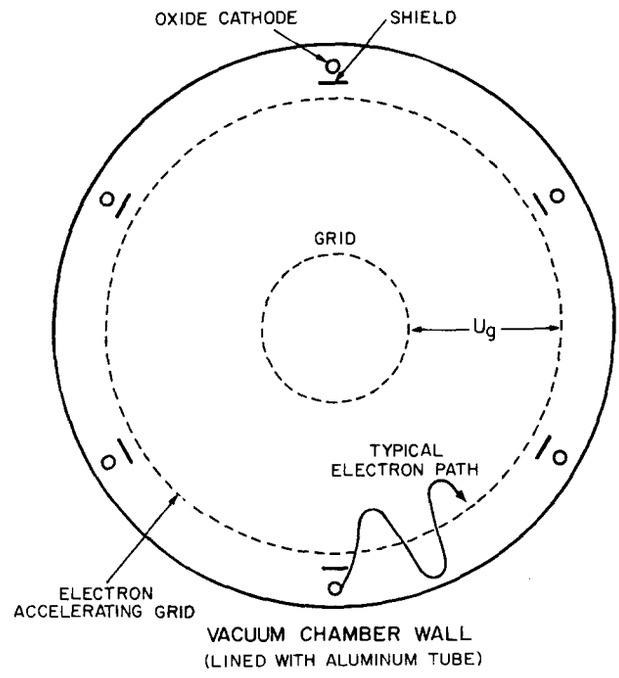

FIG. 9. Cross-sectional view of electrodes (not to scale).

TABLE I. Electrode dimensions.

	Length (cm)	Diameter (cm)	Remarks
Vacuum chamber, inside	28	15	base pressure about 4×10^{-7} Torr
Electron accelerating grid	24	10	
Grid	16	4	several different wire mesh sizes were used
Oxide cathodes	15	0.16	oxide-coated nickel tubes, heated and supported internally by a 0.08-cm-diam tungsten rod

ent theory may be inadequate to explain the experimental results of Hirsch: The solution of Poisson's equation may not be unique, the assumed distribution functions may be incorrect, and the circulating current distribution function i_1 might be discontinuous across a virtual electrode.

III. DIAGNOSTICS

The measurements of neon $1s_5$ metastable atom density were made with a laser heterodyne system operating at 0.6401 and 0.6328 μ, as shown in Fig. 8. The two He-Ne laser beams are combined at the beam splitter, and the beat frequency from the detector output is displayed on an oscilloscope. Pulsing the plasma on and off produces a change in plasma refractivity, which slightly shifts the operating frequency of the laser containing the plasma. This shift can be measured as a change in the measured beat frequency, provided that the time scale of the current pulse is short compared to the time scale for the drift of the beat frequency due to other causes, such as mirror vibrations. The minimum frequency shift which can be measured with the present system is 10 kHz, which corresponds to an average density of neon $1s_5$ metastable atoms of 1.3×10^9 cm^{-3} over the 15-cm plasma length.

The equations relating the beat frequency shift to the changes in plasma parameters are given elsewhere.[4,8] The 0.6401-μ laser wavelength is especially sensitive to the presence of neon $1s_5$ atoms, owing to anomalous dispersion from the $1s_5$–$2p_9$ transition at 0.6402 μ.[4,9] From measurements at 0.6401, 0.6328, and 3.39 μ, it was determined that the changes in ground-state neutral-atom density and electron density remained below the minimum detectable values for this system, which were 1.3×10^{13} and 2×10^{11} cm^{-3}, respectively.

In addition to the laser heterodyne measurements, the total light intensity emitted by the plasma as a function of radius was measured using a collimated photomultiplier tube. The collimator consisted of two 1-mm pinholes spaced 14 cm apart, with a baffle to minimize stray light reflection. The collimator was initially aligned parallel to the plasma axis by means of an alignment laser beam passing through the collimator to the phototube. Deuterium was used for these measurements instead of neon. With the plasma present, the light intensity at a given time in the discharge was measured

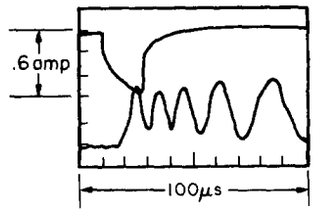

FIG. 10. Oscilloscope trace of current and laser beat signal.

during several shots at each radial position, and an average value taken. These measurements have the advantage of giving data which may be directly compared with the theoretical shape of the electron density distribution, but they do not yield the magnitude of the electron density, and the error bars are large, because of the considerable variation from shot to shot.

IV. EXPERIMENTAL DEVICE

Cylindrical geometry was chosen so that the laser beam could be aligned parallel to the axis of the plasma and moved radially to measure the radial distribution of metastable atom density. The electrodes which produced the plasma are cylinders of highly open wire mesh, arranged as shown in Fig. 9, with dimensions given in Table I.

The purpose of the cathode shields is to prevent the electrons from concentrating at those regions of the electron accelerating grid nearest the oxide cathodes, and to protect the cathodes from ion bombardment.

For Ne^+ *ion* injection into the grid, the grid was biased

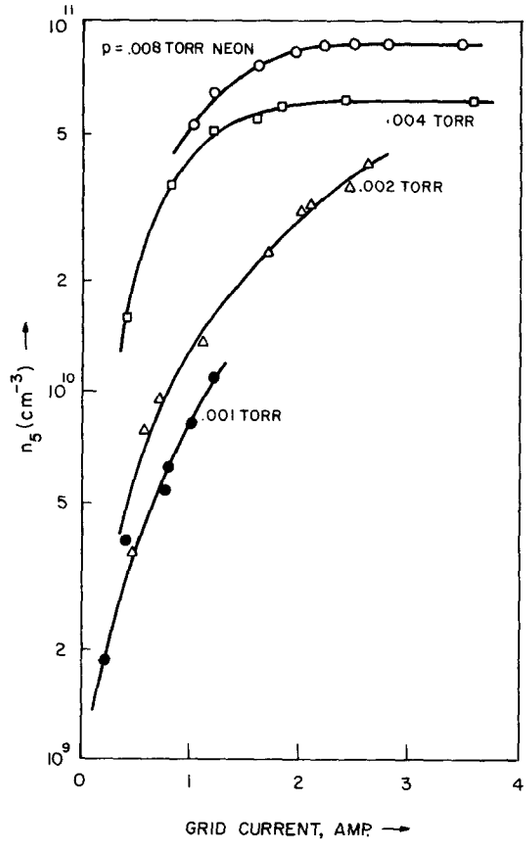

FIG. 11. Metastable density vs current.

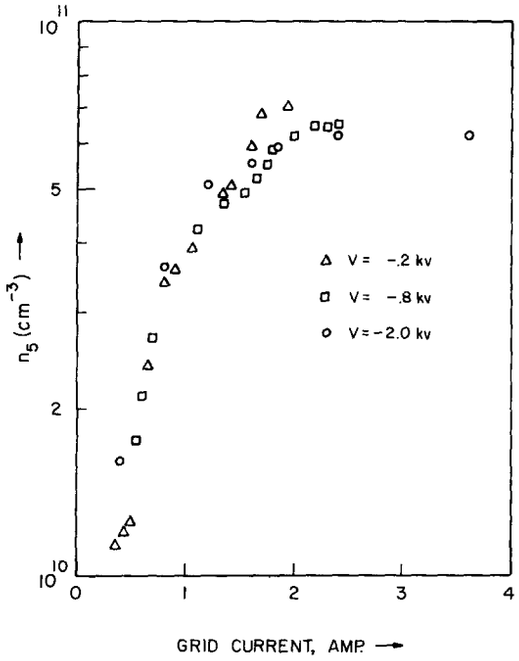

FIG. 12. Metastable density vs current at various applied voltages. (The true grid voltage is about 1000 V higher, owing to the electron accelerating grid pulser.)

negatively to a voltage between 0.2 and 5.0 kV, and the electron accelerating grid was pulsed to a positive voltage of 0.5—2.0 kV for about 20 μsec. Primary electrons from the oxide cathodes, plus any additional electrons produced by ionization, oscillate in and out of the electron accelerating grid during the pulse, ionizing the neutral neon gas. A typical electron path is sketched in Fig. 9. Neon ions formed inside the electron accelerating grid are then accelerated into the interior of the grid, producing the experimental plasma.

For *electron* injection into the grid, both grids are pulsed positive, using a voltage divider to apply a higher voltage to the center grid.

The plasma pulse is triggered when the laser beat frequency is low (around 10 kHz), and the grid current and laser beat signal are displayed on an oscilloscope trace, such as that shown in Fig. 10. In this shot, Ne^+ ions were injected into the grid at 0.8-kV grid voltage. [The grid used here was about 80% open. The time scale is 10 μsec/cm. The lower trace of the display is the laser beat signal (arbitrary amplitude units) from the 0.6401-μ laser heterodyne system. The upper trace is the grid current at 0.2 A/cm.] Here the beat frequency was less than 10 kHz when the current pulse was initiated. Then it built up to about 100 kHz at the end of the current pulse and gradually decayed after the current was shut off. Such data were taken for various radial positions, times, and experimental parameters, yielding the variations of neon $1s_5$ metastable atom density with those parameters. In order to check the theory, however, it is necessary to relate the observed metastable atom density distribution to the electron density distribution. In Sec. V the theoretical metastable density corresponding to the theoretical electron density distributions will be found as a function of radial position, time, and current; and a means of calculating the axial electron density from the measured metastable density will be derived. These relations will enable comparison of the experimental results with the results predicted by the potential theory.

V. VARIATION OF METASTABLE DENSITY WITH RADIUS, TIME, AND CURRENT

Since the metastable atoms have a long effective lifetime, their thermal motion must be taken into account in predicting where they will be at the time of observation. At the low pressures of the present work (less than 0.01 Torr), the mean free path for collisions between neutral atoms is much larger than the size of the vacuum chamber, so collisions of metastable atoms with other neutral atoms are ignored. Therefore, the diffusion equation is not valid for this case. Instead, the motion of the metastable atoms will be described by a force-free transport equation

$$\frac{\partial f(\mathbf{x}, \mathbf{y}, t)}{\partial t} + \mathbf{v} \cdot \nabla f(\mathbf{x}, \mathbf{v}, t) = S(\mathbf{x}, \mathbf{v}, t) - \nu_d f(\mathbf{x}, \mathbf{v}, y), \quad (25)$$

with the initial condition

$$f(\mathbf{x}, \mathbf{v}, 0) = 0,$$

where $f(\mathbf{x}, \mathbf{v}, t)$ is the distribution function of the metastable atoms, $\mathbf{v}$ the velocity of the metastable atom, S the source term for production of metastable atoms, and ν_d the effective collision frequency for destruction of the metastable states by electrons and ions.

The following assumptions are made: (i) Infinitely long cylinder with azimuthal symmetry; the source S is a function of radius and time only. (ii) The collisional destruction term ν_d is independent of $\mathbf{x}$ and $\mathbf{v}$. (iii) The ground-state neutral-atom density, n_0, is constant and uniform. (iv) The metastable atom density is initially

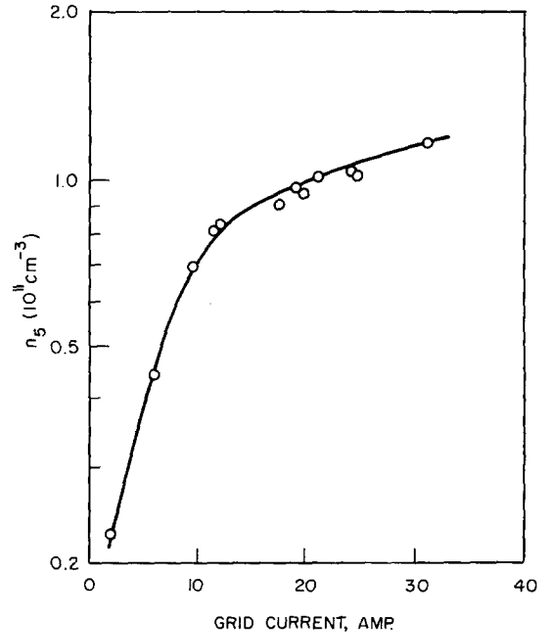

FIG. 13. Metastable density vs current for case of electron injection into the grid.

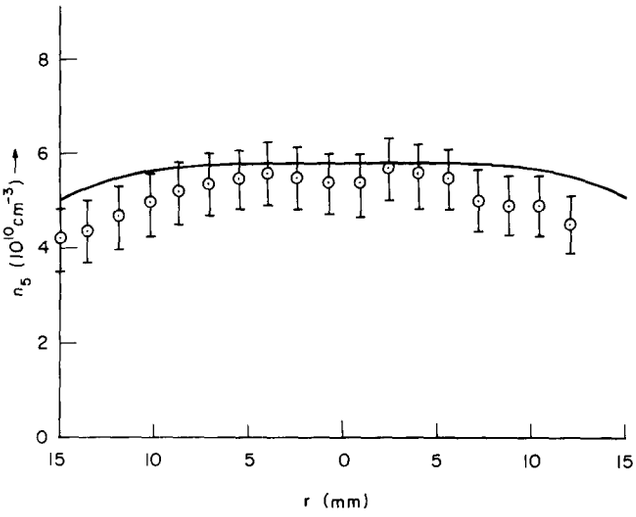

FIG. 14. Radial distribution of metastable density produced by Ne^+ ion injection, $I_1 = 4.5$ A.

zero when the current pulse is turned on at $t=0$. (v) The current pulse, and hence the source S, are constant from time $t=0$ until the end of the pulse at $t=t_1$. (vi) Free flight by metastable atoms, and all metastable atoms striking the wall are lost. (vii) A negligible amount of kinetic energy is imparted to the atom when it is excited to the $1s_5$ state. Therefore, the metastable atoms are born with isotropic Maxwellian velocity distribution characterized by

$$(\beta/\pi)^{3/2}\exp(-\beta v^2),$$

where $\beta = m_0/2kT_0$, m_0 is the neon atom mass (kg), T_0 the neutral gas temperature (deg), and k Boltzmann's constant (J deg^{-1}).

The resultant metastable atom density is found to be

$$n_5(r,t) = \left(\frac{2\beta}{r}\right)^{1/2} n_0 \int_0^\infty dr'\, r'^{1/2}\, \nu_5(r') \times \int_{(2\beta rr')^{1/2}/t}^{(2\beta rr')^{1/2}/(t-t_1)} d\rho \left[\exp\left(-\frac{\nu_d(2\beta rr')^{1/2}}{\rho} - \frac{(r^2+r'^2)\rho^2}{2rr'}\right) I_0(\rho^2)\right], \quad (26)$$

where I_0 is a modified Bessel function and ν_5 is defined below. This equation, except for the term involving ν_d, was derived in Ref. 4.

Using this equation, the theoretical radial distribution of metastable density may be found for any electron density distribution. In particular, the electron density distributions derived above will be used here. The cross section for excitation of the neon $1s_5$ states by fast Ne^+ ions is unknown, but reasonable estimations indicate that this source is negligible. Then the effective collision frequency for production of metastable atoms may be written

$$\nu_5(r) = n_e\langle\sigma_{e5}v_e\rangle, \quad (27)$$

where n_e is the electron density (m^{-3}), v_e the electron speed (m/sec), and σ_{e5} the cross section for excitation of neon $1s_5$ state from ground state by electrons. The remaining two integrations in Eq. (26) have been performed numerically on a computer, using theoretical values of n_e, yielding a theoretical radial distribution of metastable atoms for comparison with experimental data.

The time variation of metastable density is also contained in Eq. (26). Since the experimental current pulses are not truly rectangular, as was assumed, some error is introduced, but the error is less after the end of the current pulse, when the metastable atom density is decaying. It is observed experimentally that both the grid current and plasma light emission decay rapidly (in about 5 μsec) after the current pulse is shut off, so for later times the collisional destruction of metastable atoms by electrons and ions (ν_d) may be assumed negligible. Using the substitution $z = [(r^2+r'^2)/2rr']^{1/2}\rho$ in Eq. (26), setting $\nu_d = 0$ and $r=0$, and integrating over z yields the decay of the axial metastable density after the current pulse is shut off ($t > t_1$):

$$n_5(0,t) = \pi^{1/2}\beta^{1/2}n_0 \times \int_0^\infty dr'\, \nu_5(r')\{\mathrm{erf}[\beta^{1/2}r'/(t-t_1)] - \mathrm{erf}(\beta^{1/2}r'/t)\}. \quad (28)$$

This equation has been evaluated numerically, using theoretical electron density values for comparison with experimental data. It is found that, if the decay curve is approximated by an exponential function, the characteristic decay time is about 50 μsec, for the experimental gas temperature (about 400 °K).

The dependence of metastable density on current can be obtained from Eq. (26), but a simpler form can be obtained by writing an approximate rate equation for the change in metastable atom density,

$$\frac{\partial n_5}{\partial t} \sim n_0\nu_5 - n_5\left(\nu_d + \frac{1}{\tau_5}\right), \quad (29)$$

where the term n_5/τ_5 represents loss of the metastable atoms by free flight, and τ_5 is about 50 μsec. The solu-

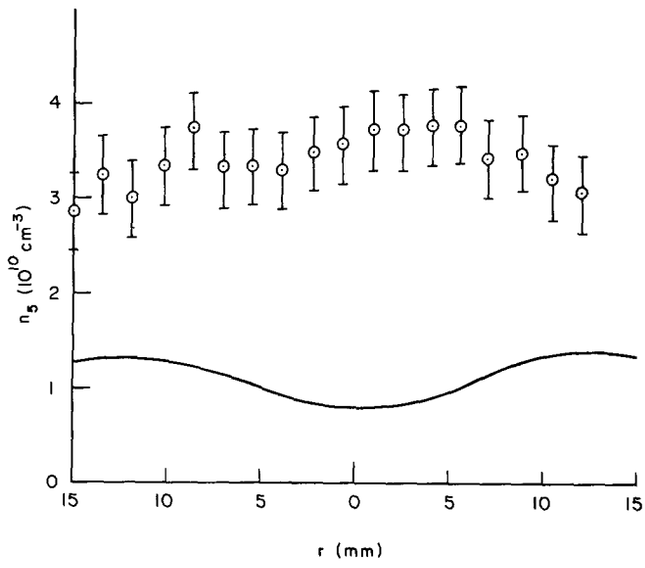

FIG. 15. Radial distribution of metastable density produced by electron injection, $I_1 = 25$ A.

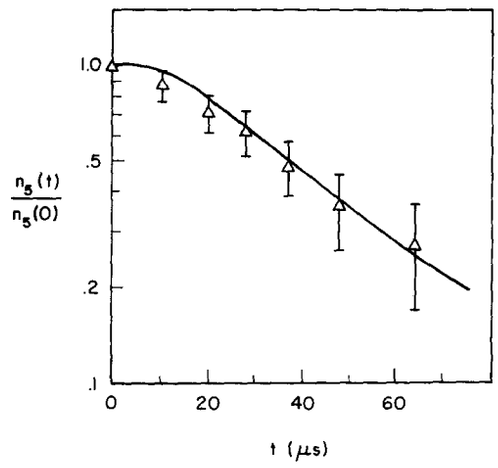

FIG. 16. Decay of axial metastable density. Solid curve—theoretical.

tion of this equation is

$$n_5(t)=\frac{n_0\nu_5}{(\nu_d+\tau_5^{-1})}\left\{1-\exp\left[-\left(\nu_d+\frac{1}{\tau_5}\right)t\right]\right\}. \tag{30}$$

The equilibrium value of metastable density is

$$n_5=n_0\nu_5/(\nu_d+\tau_5^{-1}). \tag{31}$$

At high currents (or high electron densities) $\nu_d \gg \tau_5^{-1}$, so that the metastable density reaches a saturation value defined by

$$n_{\rm sat}=\nu_5 n_0/\nu_d. \tag{32}$$

Further increases in current do not increase the metastable density beyond the saturation values, because both ν_5 and ν_d increase with current, leaving the ratio about constant. We are now in a position to estimate the electron density from measured values of metastable density, ground-state neutral-atom density, and metastable density decay time.

From Eqs. (27), (31), and (32),

$$n_5=\left(\frac{1}{n_{\rm sat}}+\frac{1}{\tau_5 n_0\langle\sigma_{e5}v_e\rangle n_e}\right)^{-1}. \tag{33}$$

This gives a means of determining the value of n_e from the experimentally measured values of metastable density and ground-state neutral-atom density.

VI. RESULTS

For the case of Ne^+ *ion* injection, the axial neon $1s_5$ density as a function of grid current is shown in Fig. 11 for various pressures at a grid voltage $U_g=-1.8$ kV. The grid used for these data had an openness of 0.87 and a spacing between grid wires of 0.6 mm. The data were all taken at the end of a 20-μsec current pulse. As the current is increased, the metastable density increases almost linearly at first and then gradually saturates at high currents. From Eq. (33), with $p=0.008$ Torr, $\tau_5=50$ μsec, and $\langle\sigma_{e5}v_e\rangle=2\times10^{-9}$ cm^3 sec^{-1}, and using measured values of $n_{\rm sat}$ and n_5, it is found that $n_e=10^{11}$ cm^{-3} at a grid current of $I=3.4$ A ($I_1\cong 20$ A). The theoretical axial electron density for these parameters is about 0.8×10^{11}, arbitrarily assuming $\lambda=0.5$ and $p_1^2=p_2^2=0.5$.

The effect of varying grid voltage is seen in Fig. 12. The points for the different voltages appear to lie close to each other, indicating little change in metastable density with voltage in this region. An increase in voltage should produce an increase in the average electron energy, and consequently an increase in $\langle\sigma_{e5}v_e\rangle$, tending to increase the observed metastable density. On the other hand, the theoretical electron density varies roughly as $U_g^{-1/2}$ at constant current, so that an increase in grid voltage would tend to produce a decrease in electron density, and, thus, in the metastable atom density. It may be that these two competing factors offset each other to produce the observed lack of variation with grid voltage, but this is not fully understood.

For the case of *electron* injection into the same grid (instead of Ne^+ ion injection) at 0.008-Torr neon, the variation of metastable density with current is shown in Fig. 13. These data were also taken at the end of a 20-μsec current pulse. Here the grid current was controlled by varying the pulsed grid voltage between 0.4 and 1.2 kV. Much higher grid currents were obtained, but the peak values of metastable density are only about 50% higher. This is a consequence of the dependence of the plasma density on the square root of the mass of the injected particle [Eq. (14)].

Measurement of the radial variation of metastable density produced by Ne^+ ion injection yielded the data of Fig. 14. These data were taken at $U_g=-1.5$ kV, at the end of a 20-μsec current pulse in neon at 0.008 Torr. Since the window aperture on the vacuum chamber is smaller than the grid diameter, part of the area inside the grid could not be viewed by the laser beam. The smooth curve is the theoretical curve computed using the theoretical electron density for the parameters of this experiment, arbitrarily assuming $\lambda=0.5$ and $p_1^2=p_2^2=0.5$. Similar data for the case of electron injection are shown in Fig. 15, at $U_g=+0.5$ kV, at the same pressure and time (20 μsec). The theoretical curve is computed assuming $\lambda=0.5$ and $p_1^2=p_2^2=0.3$.

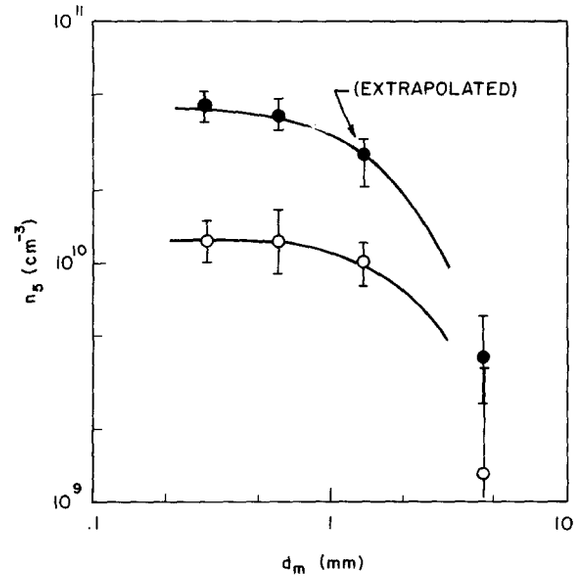

FIG. 17. Variation of axial metastable density with grid mesh size.

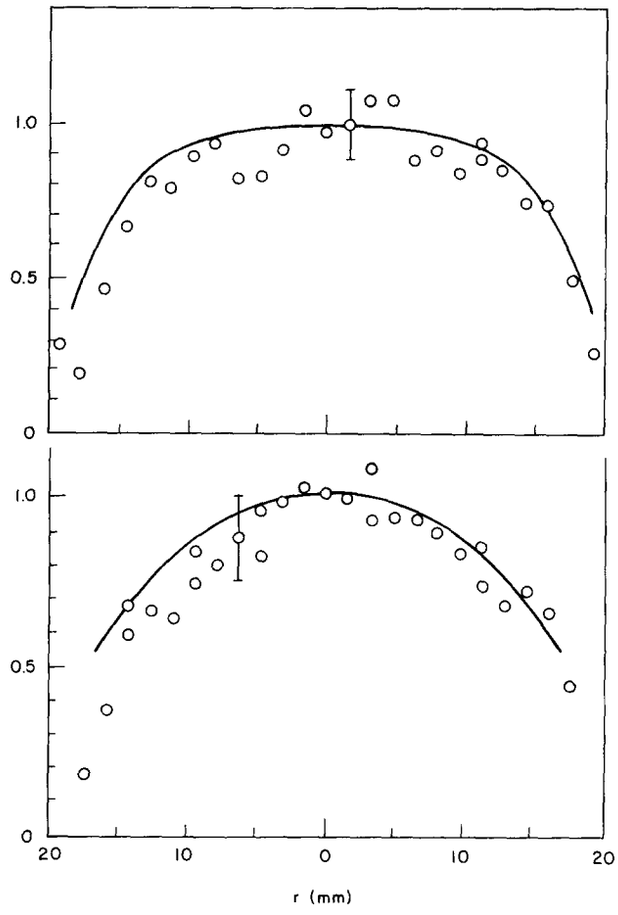

FIG. 18. Radial variation of plasma light intensity in 0.004-Torr deuterium. Upper curve: $U_g = -2$ kV and $I_1 = 2.6$ A. Lower curve: $U_g = -4$ kV and $I_1 = 3.2$ A. Smooth curves—theoretical electron density distribution, assuming $\lambda = 0.5$ and $p_1^2 = p_2^2 = 0.5$.

The decay of the axial neon $1s_5$ density is shown in Fig. 16, along with the corresponding theoretical curve from Eq. (28). These data are taken from the oscilloscope trace of Fig. 10. If the decay curve is approximated by an exponential line, the decay time τ_5 is found to be about 50 μsec.

The angular momentum of the injected particles is a very important parameter, as was shown theoretically.[4,2] The amount of angular momentum imparted to the injected particles is controlled somewhat by the spacing between wires in the wire mesh grid, especially in the presence of a plasma sheath around the grid wires. This effect was studied experimentally by using four different grids, each with a different grid mesh spacing d_m (defined as the open distance between the edges of adjacent wires). The axial neon $1s_5$ density appears to be a strong function of the mesh size, with all other parameters held constant (Fig. 17). In this figure the curves connect interpolated points of equal circulating current and pressure. For the upper curve, $I_1 = 6$ A, $p = 0.008$ Torr, and for the lower curve, $I_1 = 3$ A, $p = 0.004$ Torr. The voltage $U_g = -1.8$ kV in both cases.

The decrease in density at large mesh spacings is probably due to an increase in angular momentum imparted to the injected particles, especially when the grid wire spacing is larger than the effective shielding length of the plasma. From the location of the drop in density, this shielding length is estimated to be on the order of a millimeter, which is the Debye length for a plasma with a density of 10^{10} cm^{-3} and a temperature of a few hundred eV (although the present plasma is probably not Maxwellian).

The radial variation of total light intensity emitted by the plasma (in arbitrary units) is shown in Fig. 18 for the case of ion injection in deuterium at 0.004 Torr. For the lower curve, $U_g \sim -4$ kV, $I_1 \sim 3.2$ A and for the upper curve, $U_g \sim -2$ kV, $I_1 \sim 2.6$ A. The smooth curves are the theoretical electron density distributions, relative to the density at the center, for the given experimental parameters, assuming $\lambda = 0.5$, $p_1^2 = p_2^2 = 0.5$, $y_5 = y_7 = 0$, and $y_8 = 1$. The value of y_6 in these and previous curves is taken to be the electron accelerating grid pulser voltage (about 1 kV) divided by the magnitude of the effective grid potential U_g, which is the potential difference between the grid and the electron accelerating grid (Fig. 9).

VII. CONCLUSIONS

At very low current the potential well is shallow and round, but at higher current it is deep with a broad flat minimum. The axial plasma density increases almost linearly with current and also increases with radial focusing, i.e., decreasing angular momentum.

The laser heterodyne system at 0.6401 and 0.6328 μ permits determination of the density of neon atoms in the $1s_5$ metastable state (10^9—10^{12} cm^{-3}) in a plasma as functions of space, time, and experimental parameters, with an accuracy of about 10—20%.

The observed saturation of the metastable density at high currents is attributed to collisional destruction of the metastable states. The radial distributions of metastable atom density have shapes similar to those predicted theoretically, but the magnitudes are dependent upon the unknown values of trapped current and angular momentum.

The peak experimental electron density is 10^{11} cm^{-3} at a circulating current of $I_1 \sim 20$ A. This value is compatible with the values predicted theoretically assuming rectangular distributions of total energy and angular momentum.

The decay of the axial metastable density after the current pulse is shut off is consistent with the theoretical curve based on the above assumptions.

The marked decrease in metastable density at grid mesh spacings larger than 1 mm is attributed to the presence of a plasma sheath around the grid wires, which increases the amount of angular momentum imparted to the injected particles, decreasing the confined density.

The radial variation of emitted light intensity has a shape similar to the theoretical electron density distribution for the given experimental conditions.

In general, the theoretical predictions based on electron density distributions from the assumed rectangular distributions are consistent with the experimental results.

*Work based upon Ph.D thesis submitted by T. J. Dolan, University of Illinois. Supported by the Air Force Office of Scientific Research.
†Present address: Nuclear Engineering Department, University of Missouri, Rolla, Mo. 65401.
[1]W. C. Elmore, J. L. Tuck, and K. M. Watson, Phys. Fluids 2 (No. 3), 239 (1959).
[2]O. A. Lavrent'yev, *Magnitnye Lovushki*, vypusk 3 (Nankova Dumka, Kiev, U.S.S.R., 1968), pp. 77—147. [Atomic Energy Commission Report No. AEC-tr-7002, 1970 (unpublished).]
[3]R. L. Hirsch, J. Appl. Phys. 38, 4522 (1967).
[4]T. Dolan, Ph.D. thesis (University of Illinois, 1970) (unpublished).
[5]C. W. Barnes, Stanford University Institute for Plasma Research Report No. 344, 1970 (unpublished).
[6]D. A. Dunn, Ninth Annual Meeting of the Division of Plasma Physics of the American Physical Society, Austin, Texas, 1967, Paper No. 3E-11 (unpublished).
[7]A. Ralston, *A First Course in Numerical Analysis* (McGraw-Hill, New York, 1965).
[8]J. T. Verdeyen, B. E. Cherrington, and M. E. Fein, Appl. Phys. Letters 2, 360 (1966).
[9]L. A. Schlie and J. T. Verdeyen, IEEE J. Quantum Electron. QE-5, 21 (1969).

Oxygen-Processed Field Emission Source*

Lee H. Veneklasen† and Benjamin M. Siegel
Department of Applied and Engineering Physics, Cornell University, Ithaca, New York 14850
(Received 1 June 1971; in final form 1 November 1971)

An oxygen-enhanced thermal-field shaping method has been developed for obtaining high angular confinement of the electron emission from a ⟨100⟩-oriented tungsten tip. A source is obtained from which the beam is confined to a half-angle of ~0.15 rad. This strongly-forward-direction beam gives a source that can be used to obtain beams with currents as high as 5×10^{-8} A within an acceptance angle of 5×10^{-3} rad with a total emission curve of only 10 μA. The processed tip is operated at 900 °C to give a source with long-term stability and reliability in a moderate ultrahigh vacuum of $\sim10^{-9}$ Torr. Energy spread and flicker noise are slightly greater than for a "clean" tip operating at room temperature, but remain favorable for many applications. An interpretation of the shaping of the tip based on field-induced thermal migration is given.

INTRODUCTION

The field emission source with its small size, high current density, and narrow energy spread offers major advantages in electron beam equipment requiring high brightness and coherence. Such a source has been very successfully applied to high-resolution scanning transmission electron microscopy by Crewe and co-workers.[1–3] It is the prototype being used by other workers in proposed electron optical instrumentation. The future should see important applications in transmission electron microscopy,[4,5] electron diffraction, holography, microrecording, and other electron probe instrumentation.

Adapting a field emission source to electron optical applications requires a stable source that can operate in a moderate ultrahigh vacuum and give an intense beam of very high brightness with a minimum total emission current. The aberrations of the beam forming optics generally set the limit of the angular aperture that can be accepted from the field emission source without a deterioration of its effective brightness and coherence. The vacuum conditions, physical radius of the tip, emission current, and temperature of the tip determine the stability, effective radius, energy spread, and beam noise of the field emitter.

Swanson and Crouser[6] have discussed the implication of angular confinement of the electron beam for obtaining high-brightness high-coherence sources. This confinement is accomplished by either selectively reducing the work function of specific lattice planes or by developing locally sharper regions on the emitter by field-enhanced buildup or field evaporation of the tip. As they have shown, the greatest angular beam confinement can be obtained using a ⟨100⟩-oriented tungsten tip.

Reduction of the work function of the (100) lattice plane on the tungsten tip has been obtained by evaporation of a zirconium-oxide layer.[7,8] An evaporated monolayer of beryllium has also been shown to lower the work function of tungsten, but here the enhanced emission occurs from the (011) facet.[9] Deposition of material on the emitter to lower the work function can produce field emission sources giving higher current densities and higher ultimate brightness than clean emitters[6] with the possibilities of more stable and less noisy operation at lower total emission currents. But these advantages must be paid for by an inconvenient evaporation process in the electron optical system.

High-temperature field evaporation of a ⟨100⟩-oriented emitter would be a reliable method of producing beam confinement. This method requires a high reverse voltage for processing and yields a smaller reduction in beam voltage than the other methods, making it less suitable for the electron optical applications in which we are most interested. Field-induced migration of tungsten to reform the shape of a clean tungsten tip has been investigated by Bettler and Charbonnier.[10] Different combinations of reverse-bias voltage and temperature promote buildup on the (310), (211), or (100) lattice planes. Using thermal-field buildup of a ⟨100⟩-oriented tungsten tip, Swanson and Crouser[6] have obtained beams confined to average emission angles of 0.1—0.3 rad with beam voltages reduced as much as 50%. Crewe and co-workers[2] have used thermal field remolding of ⟨310⟩-oriented tips to obtain similar enhancement in their field emission source for application in the scanning transmission electron microscope. These tips are op-